The manuscript is a preprint uploaded to EarthArxiv. This preprint will be submitted to *Solid Earth*. Authors encourage downloading the latest manuscript version from EarthArXiv, and welcome comments feedback and discussion anytime.

Please feel free to get in contact: utsav.mannu@iitgn.ac.in

Thrusts control the thermal maturity of accreted sediments

Utsav Mannu[1,*], David Fernández-Blanco[2], Ayumu Miyakawa[3], Taras Gerya[4], and Masataka Kinoshita[5]

[1]Discipline of Earth Sciences, Indian Institute of Technology, Gandhinagar, India

[2] Barcelona Center of Subsurface Imaging, Institut de Ciències del Mar (ICM-CSIC), Barcelona, Spain;

[3]Geological Survey of Japan, AIST

[4]Institute of Geophysics, ETH Zurich

[5]Earthquake Research Institute, UTokyo

Correspondence to: Utsav Mannu (utsav.mannu@iitgn.ac.in)

Abstract. Thermal maturity assessments of hydrocarbon-generation potential and thermal history rarely consider how upper-plate structures developing during subduction influence the trajectories of accreted sediments. Our thermomechanical models of subduction support that thrusts evolving under variable sedimentation rates and décollement strengths fundamentally influence the trajectory, temperature, and thermal maturity of accreting sediments. This is notably true for the frontal thrust, which pervasively partitions sediments along a low and a high maturity path. Our findings imply that interpretations of the distribution of thermal maturity cannot be detached from accounts of the length and frequency of thrusts and their controlling factors. Taking these factors into consideration, our approach provides a robust uncertainty estimate in maximum exposure temperatures as a function of vitrinite reflectance and burial depth thereby reducing former inconsistencies between predicted and factual thermal maturity distributions in accretionary wedges.

1. Introduction

Organic material transforms into coal, oil, and gas at rates primarily controlled by temperature(Quigley & Mackenzie, 1988). This transformation, critical for the hydrocarbon industry, is also useful to study the tectonic and sedimentary evolution of basins and orogens (Tissot et al., 1987; Tissot & Welte, 2013; Waples, 1981). The extent of this transformation in sediments, known as thermal maturity, can be measured as vitrinite reflectance; the percentage of incident light reflected from the surface of vitrinite particles in those sediments (Burnham & Sweeney, 1989). Thermal maturity has been used to estimate the thermal evolution of igneous intrusions(Bostick & Pawlewicz, 1984) and seismic slip(Rabinowitz et al., 2020), the extent of diagenesis and low-grade metamorphism(Ferreiro Mählmann & Le Bayon, 2016; Totten & Blatt, 1993), porosity and compaction in basin sediments (Schmoker & Gautier, 1988), as well as the geothermal history of accreting material during subduction (A. Sakaguchi et al., 2011; Underwood et al., 1992; Yamamoto et al., 2017).

Inferences on the geothermal history of subduction margins based on thermal maturity depend on the trajectory followed by the accreting sediments (Miyakawa et al., 2019). Low-temperature high-pressure metamorphic rocks in the subduction wedge are often attributed to the pressure maxima that typically predate the temperature maxima in sediments accreted in the wedge (Platt, 1993). However, numerical models (Ruh, 2020b) and field observations(Giunchi & Ricard, 1999) have indicated the existence of complicated patterns in sediment trajectories. As the orogenic wedge evolves, sediments accreting along different paths reach different depths and velocities and are exposed to different regional peak temperatures. Miyakawa (2019) proposed to subdivide these trajectories based on their final characteristics such as thermal maturity. As a result, the spatiotemporal evolution of the sediments which regulate thermal maturity is controlled, to a first-order, by the partition of incoming sediments along two end-member pathways; (i) a deeper path leading to elevated thermal maturities, the ***high thermal-maturity path***, and (ii) a shallower path resulting in low thermal maturity, the ***low thermal-maturity path*** (Miyakawa et al., 2019).

Although a number of researchers have studied the diversity of particle paths by their Pressure-Temperature evolution in accreted and underthrusted sediments, in presence of surface processes, distribution of surface processes, in both

analytical and numerical models(Hori & Sakaguchi, 2011; Elena Konstantinovskaia & Malavieille, 2005; Platt, 1986; Ruh, 2020a; Wenk & Huhn, 2013), its correlation or lack thereof with its pre-accreted state has not been suitably investigated. Much remains to be explored regarding how the partition of high/low thermal maturity paths and the general translation of sediments occurs inside the wedge, given the conventional assumption that accreting sediments remain at the same relative depth (Hori & Sakaguchi, 2011) and translate along the adjacent "layers" without vertical mixing throughout the tectonic evolution of the wedge (Luján et al., 2010; S. Willett et al., 1993) to yield this diversity of sediment paths. To better understand the time-depth paths of wedge sediments, their dependence on the initial state of undeformed sediments, and thus their thermal maturity, the factors that control the evolution of subduction-accretion systems, like sedimentation, erosion, and décollement strength (Mannu et al., 2016; Simpson, 2010), ought to be considered.

Here, we explore in detail the impact that a realistic account of accretion in a subduction wedge has on the thermal maturity of its sediments. We simulate subduction-accretion using 2D finite-difference thermomechanical models incorporating empirical thermal conductivity values from the Nankai accretionary margin. We track the evolution of thermal maturity by computing vitrinite reflectance($\%R_0$) using three well established methods of $\%R_0$ computation, on each marker in the model as the wedge develops by accretion under different sedimentation rates and décollement strengths. These factors notably alter the trajectories and thermal maturities of incoming sediments. Particularly, thrusts define sharp thermal maturity boundaries leading to stark differences in the thermal maturity of sediments that accrete in different thrust blocks, even when they follow similar trajectories and lay nearby.

2. Methods

We employ I2VIS, a conservative (Gerya, 2019) finite-difference 2‑D thermomechanical subduction-accretion model with visco-plastic/brittle rheology (Gerya & Yuen, 2003). The code solves the governing equations for conservation of mass, momentum, and heat as well as the advection equation with a non-diffusive marker-in-cell scheme (Gerya, 2019) constrained by thermal conductivity values inferred from Nankai accretionary wedge (Sugihara et al., 2014). Our numerical approach has several advantages over earlier models to simulate thermal maturity in an accretionary wedge(Miyakawa et al., 2019), such

as a more realistic geothermal profile, variable particle paths, and thermal evolution. The supplementary material contains information regarding the governing equations, the modified thermal conductivity formulations based on the C0002 borehole in the Nankai accretionary wedge, boundary conditions, the rheological model, model setup (Fig S1) and surface processes(Fig S2).

2.1 An improved thermal maturity calculation

Given that assessments of thermal maturity are inherently reliant on the distribution of temperature inside the wedge, any attempt to model thermal maturity needs a realistic temperature gradient in the wedge. We incorporate this by modifying the thermal conductivity computation for sediments and décollement (see Table 1 and section 1 in the provided supplementary text) to match the empirical relationship between depth and thermal conductivity, as measured on core samples in the borehole IODP Site C0002(Sugihara et al., 2014; Tobin et al., 2015). Both for the same accretionary wedge is scarce to find, and to our knowledge, the C0002 borehole in Nankai accretionary wedge along the Kumano forearc basin is the only place with available datasets for both thermal conductivity and thermal maturity values for an accretionary wedge (Fukuchi et al., 2017). The model computes the $\%R_0$ of each marker to estimate the thermal maturity of sediments during the model run using three widely used methods of thermal maturity modelling Easy$\%R_0$ (Burnham & Sweeney, 1989), Simple$\%R_0$(Suzuki et al., 1993) and Basin$\%R_0$ (Nielsen et al., 2017). All these approaches for computing $\%R_0$ yield similar trends albeit different absolute values. In the interest of clarity, we have mostly illustrated Easy$\%R_0$, which is the most extensively used method for Vitrinite Reflectance computation. Hence, in the interest of clarity, we have mostly illustrated Easy$\%R_0$, which is the most extensively used method of Vitrinite Reflectance computation. Hence, hereafter we refer Easy$\%R_0$ as simply $\%R_0$, unless explicitly stated. $\%R_0$ is set to 0.2 in sediment markers at the start of the model till 2.5 Myr, while $\%R_0$ in markers for other rocks, air, and water is undefined at all times. After 2.5 Myr, the model computes $\%R_0$ on each marker as a function of temperature (T), time (t), and amount of fixed carbon as a percentage(f_c). The initial $\%R_0$ of newly deposited sediments is computed using an assumed water-sediment interaction temperature assumed to be the same as the thermocline. The thermocline used in the model has been estimated using the data obtained and made freely available by International Argo Program and the national programs that contribute to it for the region near Nankai (Argo, 2022). is set to 0.2 in sediment markers at the start of the model till 2.5 Myr, while $\%R_0$ in markers for other rocks, air, and water is undefined at all times.

After 2.5 Myr, the model computes $\%R_0$ on each marker as a function of temperature (T), time (t), and amount of fixed carbon as a percentage(f_c). The initial $\%R_0$ of newly deposited sediments is computed using a water-sediment interaction temperature assumed to be the same as the thermocline. The thermocline used in the model has been estimated using the data obtained and made freely available by International Argo Program and the national programs that contribute to it for the region near Nankai (Fig S3, Argo, 2022).

2.2 Experimental Strategy

Here, we present a total of 10 models that vary in their effective basal friction or their effective sedimentation rate to discern patterns of thermal maturity evolution in wedge sediments. Models M_0^2, M_0^7, M_0^{12}, M_0^{17}, M_0^{22}, have no sedimentation and effective internal angle values for the décollement of ϕ_b= 2°, 7°, 12°,17° and 22° respectively. The chosen range of effective decollement strength is well within the range of values postulated by several studies for the Nankai accretionary wedge(Tesei et al., 2015). The rest of the models shown here, $M_{0.1}^{12}$, $M_{0.3}^{12}$, $M_{0.5}^{12}$, $M_{0.7}^{12}$, and $M_{0.9}^{12}$ have a medium-strength décollement and variable effective sedimentation rate ranging from 0.1 to 0.9 mm/yr. Sedimentation occurs only at the trench in all of the models presented in this study from sea to land. With these models, we evaluate the particle trajectory and $\%R_0$ of accreting sediments as a function of décollement strength (M_0^2-M_0^{22}) and sedimentation rate ($M_{0.1}^{12}$-$M_{0.9}^{12}$). To restrict the number of parameters influencing our observations, models have no erosion. . Moreover, all models lack surface processes during the first ~2.5 Myr and have sedimentation thereafter. Sediments used in the model have an angle of friction of 30° and a strain-softened value of 20° after a threshold of 0.5-1.5 strain. The coefficient of friction increases linearly between the thresholds. Sedimentation rates are the effective sedimentation rate computed after the model run and are thus not prescribed a priori. This choice ensures that the range of average sedimentation in all our models (0.1-0.9 mm/yr) lies within observed sedimentation rates in our chosen natural equivalent, the Nankai accretionary wedge in the south-western subduction margin of Japan(Korup et al., 2014). Table 2 provides more details about the model run and prescribed sedimentary conditions.

3. Results

Subduction begins at 0.1 Myr as the weak material between continental and oceanic plate fails (see supporting information movies). Continued and sustained accretion of sediments against the deforming continental crust forms the accretionary wedge from the interplate contact landwards. After ~5 Myr, all models develop a distinct wedge in agreement with the critical taper theory(Davis et al., 1983). Taper angles increase systematically as effective basal friction increases from ~2° to ~22° (Fig 1, Table 2, $M_0^2 - M_0^{22}$). Whereas models with a relatively weaker décollement, as M_0^2 (ϕ_b= 2°), have taper slopes of 4.3°± 0.3°, models with very strong décollement, as M_0^{22} (ϕ_b= 22°), have slopes as steep as 12.8 ± 1.2°(Table 2). Models without trench sedimentation grow solely by accretion of incoming seafloor sediments, with frequent nucleation of frontal thrusts. Models with weaker décollements develop thrusts that are the lengthier and remain active for shorter periods. This is clear when comparing, for models with increasingly strong décollement $M_0^2 - M_0^{22}$, the average distance between first and second frontal thrusts are 15.5 ± 7.0 km, 12.1 ± 3.6 km, 8.8 ± 3.3 km, 8.7 ± 2.1 km and 8.0 ± 1.8 km, respectively. Increasing sedimentation rate also leads to an increase in thrust sheet length from 7.3± 1.1 km in $M_{0.1}^{12}$ to 13.8 ± 7.8 km in $M_{0.9}^{12}$. In models with similar basal friction, models with higher sedimentation rates have lengthier thrust sheets that remain active for longer periods (Table 2). Steeper surface slopes with increased décollement strengths and change in thrush sheet length with sedimentation and décollement strength are well-known effects that have been confirmed by previous numerical (Mannu et al., 2016; Wang & He, 1999) and analytical(Malavieille & Trullenque, 2009; Storti & Mcclay, 1995) models. All the reported values are mean ± Standard Deviation values recorded between 2.5-7.5 Myr in individual models. All models, exhibit a temperature gradient that corresponds well with the temperature profile observed in the boreholes at IODP Site C0002 in the Kumano forearc basin, on top of the Nankai accretionary wedge (Fig. S4).

3.1 Thermal maturity of the wedge

Sediments are more thermally mature in wedges that have a higher sedimentation rate or décollement strength. For example, the mean $\%R_0$ of simulations for wedges with highest sedimentation ($M_{0.9}^{12}$) is 12% higher (0.75) than in those without

sedimentation (M_0^2) (Table 2, Fig 1). Similarly, simulations of wedges with the strongest décollement have the highest mean $\%R_0$ (0.94) of all the simulations presented in this study.

Thermal maturity values increase with depth and landward distance from the trench to the forearc high irrespective of the decollement strength, sedimentation rates and method of thermal maturity computation (Fig. 1). As a result, sediments at the core of the wedge consistently reach the highest maturity. The absolute value of $\%R_0$ and the rate at which thermal maturity values increase landward from the trench are larger for wedges with high décollement strength(Fig. 2A). In wedges with same décollement strength but higher trench sedimentation the rate of thermal maturity increase landward from the trench remain very similar(Fig. 2B). Comparing the values of $\%R_0$ (Fig. 2) along an arbitrary horizon in several models emphasizes this result; the model with the highest décollement strength attains the maximum $\%R_0$ of 1.25, and has the highest rate of landward increase in thermal maturity(Fig. 2A). However, all models with similar décollement strength but different sedimentation donot visibly vary in their rate or magnitude of landward increase in thermal maturity. All models show a decrease in thermal maturity landward of the forearc high, commonly of 0.2 $\%R_0$. Other interesting observations that we explore below are the increased thermal maturity occurring in the vicinity of thrusts (e.g. Fig 1) and the reversal in sediment maturity around out-of-sequence thrust (e.g. Fig 1) active over longer times visible across several models (Fig 1).

The magnitude of $\%R_0$ varies consistently among Easy$\%R_0$, Simple$\%R_0$ and Basin$\%R_0$. On an average Easy$\%R_0$ have the smallest values, followed very closely by Basin$\%R_0$(with an average difference of only 0.02). However, Simple$\%R_0$ had the highest average value of thermal maturity being 0.16 and 0.13 higher than Easy$\%R_0$ and Basin$\%R_0$ (Fig 1).

3.2 Sediment trajectory inside the wedge

Sediments follow high-maturity paths in larger proportions in wedges with a higher décollement strength or sedimentation rate. We demonstrate this effect by creating a map of the thermal maturity of sediments at 7.5 Myr of the model run, mapped to their spatial position 5 Myr earlier (at 2.5 My of the model run) (Fig. 3) to analyse the spatial correlation between sediment position (depth and distance) from the trench and thermal maturity. We also show the mean thermal maturity attained by sediments at a given horizontal distance from the trench during this period. The scatter plot shows sharp changes

with distance from the trench that relate to changes in sediment trajectory (Fig. 3). The mean thermal maturity is also variable along the horizontal length of the wedge and has a periodicity increasing in distance with higher sedimentation rate but relatively constant with changing basal friction (Fig. 3). Whereas the mean thermal maturity has a short periodicity of ~7.2 km for the model M_0^{12} with no sedimentation rates, the model $M_{0.9}^{12}$ shows the longest periodicity of 21 km. However, for all models with the same no sedimentation M_0^2-M_0^{22} the periodicity remains relatively consistent between the range of 7-8 km.

Fig 3 also represents the distribution of trajectories that exist in an accretionary wedge and how these trajectories get impacted under trench sedimentation(a subset of these trajectories can be viewed in the supplementary Fig. S5). Whereas in wedges with weak decollements (M_0^2), none of the shallowest half of incoming sediments reach $\%R_0 > 1$ in 5 Myr, 2% of sediments reach this value in wedges with strong décollement (M_0^{22}). The effects of décollement strength in the thermal maturity of sediments can be quantified as well at deeper levels, with one-eighth vs more than half of the sediments surpassing values of $\%R_0 = 1$ for the deepest half of incoming sediments (12.0% and 54% respectively) in weak vs strong-decollement wedges(M_0^2 vs M_0^{22}), respectively. Increasing the sedimentation rate shows this effect even more prominently. In wedges from the model without sedimentation(M_0^{12}), none of the top half m of sediments yield $\%R_0 > 1$, while ~ 15% of them surpass $\%R_0 > 1$ in the models with a sedimentation rate of 0.9 mm/yr ($M_{0.9}^{12}$). In sum, the proportion of sediments in the top half and bottom half of the wedge that reach high maturity steadily increases with both sedimentation rate and décollement strength (Table 2).

3.3 Patterns of trajectory and thermal maturity in incoming sediments

The diversity in the trajectory of sediments in the wedge leads to a plethora of pathways in which the sediments can become thermally mature and thus introduces epistemic uncertainty in the estimation of maximum exposure temperature. Fig 4, captures this uncertainty where we plot the maximum exposure temperature as a function of $\%R_0$ for all the models simulated in this study. We find that almost all the models show a remarkable similarity in their relationship between maximum exposure temperature and $\%R_0$ (for individual models please see Fig S6) and differ mostly in their proportion of

sediments with extreme values of $\%R_0$. We observe that the typical uncertainty in maximum exposure temperature increases with an increase in values of $\%R_0$ with ~ 15℃ interval at around $\%R_0$=0.2 compared to ~33℃ interval at $\%R_0$= 3 (both for 95% confidence interval, Fig. 4b). Furthermore, we observe that information about the present depth of the sediments w.r.t the thickness of the wedge (as represented by different colours in Fig 4a) greatly helps to further constrain the maximum exposure temperature. For instance, although the overall uncertainty at $\%R_0$=1, for is ~23℃, for sediments with a normalized depth of 0.2-0.4, the uncertainty greatly reduces to only ~10.5℃. Thus the range of thermal maturity values for sediments clearly has a large correlation with their trajectories.

3.4 Comparision of Easy$\%R_0$ Simple$\%R_0$ and Basin$\%R_0$

Finally as our models produced three sets of $\%R_0$ using Easy$\%R_0$(referred to as $R_0\%$ throughout our study), Simple$\%R_0$ and Basin$\%R_0$, it also gives us a unique perspective on comparative advantages of each method. Uncertainty for all three models increases with increasing $\%R_0$ from ~20–25℃ at ~0.3 which rises to ~35℃ at $R_0\%$=3.5(Fig 4b). Easy$\%R_0$ is the most well-recognised method of thermal maturity computation and yields the best constraint on uncertainty for very small changes around the values less than 1. For the values of $\%R_0$ between 1 and 3, all models yield very similar uncertainty, with Simple$\%R_0$ yielding the most constrained exposure temperatures(Fig 4b). However, beyond $R_0\%$=3, the Simple$\%R_0$ becomes highly unreliable, with uncertainty in exposure temperatures as high as 55℃ at $R_0\%$=4. Easy$\%R_0$ yields a reasonable uncertainty range of ~37℃ till $R_0\%$=4.4, but starts to be unreliable above this value. Basin$\%R_0$ remains consistent till a very high value of $R_0\%$(~6), and thus provides the best constraint on the widest range of values of thermal maturity(Fig 4b).

4. Discussion

Our models achieve realistic thermal maturity distributions thanks to unique computational advantages over models in the previous studies(Mannu et al., 2016, 2017; Miyakawa et al., 2019), despite several relevant assumptions. Models are simplified by assuming no elasticity, predefined décollement, no erosion, and using simple and uniform rheology, and either has an insufficient resolution or lack empirical relations to simulate the compaction of sediments and processes of multiscale

fluid flow. Although these assumptions hinder a wholesale comparison between our simulations and natural examples of accretionary wedges, we are confident of the thermal maturity patterns of our models. Our estimated $\%R_0$ values for the model $M_{0.1}^{12} - M_{0.9}^{12}$ are in very good agreement with the $\%R_0$ values measured for the borehole C0002 Nankai accretionary wedge (used for thermal conductivity values) by Fukuchi et. al. 2009 (Figure 5). Moreover, the temperature estimated from the observed thermal maturity of a timeframe of 1-2 Myr in the borehole, also strongly correlates with the trend and the range of 95% Confidence interval of T vs $\%R_0$ estimated in our models (Fig S7). Furthermore, our models also correlate with the patterns of P-wave velocity for Nankai(Górszczyk et al., 2019; Nakanishi et al., 2018) and Hikurangi(Arai et al., 2020) margins(Dewing & Sanei, 2009). Models compute realistic thermal maturity distributions thanks to several key improvements. Firstly, our models calculate temperature gradients that evolve at long time intervals and thus closely replicate accretionary wedges in nature (Fig. S2). This enables the simulation of realistic temperature profiles based on thermal conductivity values derived empirically from natural accretionary wedges, as in our case, the Nankai margin(Sugihara et al., 2014) Secondly, our simulations account for the effects that thermal and isostatic feedback from the oceanic lithosphere have on the evolution of the wedge by simulating plate subduction at a large scale rather than just the accretionary wedge(Miyakawa et al., 2019). Finally, our method calculates the vitrinite reflectance of sediments on each marker of the model. This capacity to accurately estimate thermal maturity in each marker informs the research questions of this study and allows inferences beyond those of depth-dependent thermal maturity distributions.

The thermal maturity of the wedge increases landward, as signalled by the landward increase in $\%R_0$ (Fig. 1). This has been observed in natural accretionary wedges such as Miura–Boso plate subduction margin (Yamamoto et al., 2017), fold and thrust belts Western Foothills complex in western Taiwan (Arito Sakaguchi et al., 2007) and other numerical models of accretion(Miyakawa et al., 2019), resulting from the long-term deformation of older accreted sediments and the backstop-forced exhumation in the wedge. Our models show that the rate of landward rise in thermal maturity is faster for thicker wedges (Fig 2). This is the case for wedges with high basal strength(M_0^{22}), for sediments in thicker wedges deform more prominently than those in their thinner counterparts. Simulations also show that sediments reach deeper levels in thicker wedges and that this increases the overall thermal maturity of the wedge. Also, increased exhumation rates and steeper thermal maturity gradients occur in the wedge interior, as the continental backstop deflects sediment trajectories

upwards during accretion (Fig. 2). As a result, for the geometry of the backstop used in our models, backstop-forced exhumed material is, on average, thermally more mature.

Our models expose two relevant cases where the increase of thermal maturity with depth or landward is relevantly altered: on-fault increase and fault-block inversion. Our models attest to the steep rise in thermal maturity of sediments at fault sites (Fig. 1). This is well documented in nature, as for boreholes C0004(Sakaguchi et al., 2011). However, on-fault increases in thermal maturity are comparatively smaller in our simulations and lack the marked increase in $\%R_0$ observed at fault sites in nature. This is primarily due to our models developing wider fault zones than their natural equivalents and the subsequent acceleration in the thermal diffusion occurring in simulated thrusts. During fault-block inversions, the positive gradient of thermal maturity with depth is inverted by thrusting relatively mature sediments over less mature sediments(Underwood et al., 1992). This is known from natural observations, as along the Fukase Fault in Shimanto accretionary wedge(Ohmori et al., 1997) and underneath the forearc basin in Nankai accretionary wedge(Fukuchi et al., 2017), and previous modelling efforts(Miyakawa et al., 2019).

Collation of the above implies that the thermal maturity of accretionary wedges results from the general increase of thermal maturity (i) with depth and (ii) landward, as well as from its (iii) modification by thrust faults. Our models suggest thermal maturity inversions by thrusting, which are commonplace in accretionary contexts, are the primary cause of thermal maturity differentiation among wedges with initially similar geothermal gradients. In other words, the strong differentiation in the trajectory of sediments led by thrusting has a larger influence over thermal maturity than burial depth or in-wedge location. This novel inference has probably remained concealed thus far due to the large number of parameters that condition thrust development, frequency, length, and thermal state. Influencing parameters to include sedimentation, erosion, basal friction and relief, pore pressure and fluid state, wedge length and thickness, taper angle, and many others(Dominguez et al., 2000; E. Konstantinovskaia, 2005; Mannu et al., 2016; Ruh, 2017; Simpson, 2010; H. J. Tobin & Saffer, 2009). It is nevertheless important to note that the frequency of faults in a wedge can be impacted by many other factors, including hinterland sedimentation(Simpson, 2010; Storti & Mcclay, 1995), erosion(E. Konstantinovskaia, 2005; S. D. Willett, 1999), and seafloor topography(Dominguez et al., 2000). Below, we discuss how thrusts not only alter the thermal evolution of accreting sediments but are, in fact, the primary control of their thermal maturity.

Thermal maturity correlates with sediment depth weakly near faults and more strongly away from them. The distance of sediment from frontal thrust dictates the trajectory of sediment grains, and as a result, the pressure-temperature conditions to which they are exposed. In this study, we have considered solely how décollement strength and the rate of trench sedimentation vary the frequency, architecture, and overall behaviour of thrusts, and the frontal thrust, as the wedge evolves. Our results show the need to consider all factors influencing fault frequency when inferring the geothermal history of contractional terrains by means of thermal maturity. Fortunately, this predictive exercise should be relatively straightforward, for the impact of these external factors on the fault structure of wedges has been established(Fillon et al., 2012; Mannu et al., 2016, 2017; Mugnier et al., 1997; Simpson, 2010; Storti & Mcclay, 1995), and the effect of each of these factors can be accounted for when assessing the trajectory of sediments and the distribution of thermal maturity in accretionary wedges.

Sediment mixing in subduction wedges is primarily controlled by thrusting. Previous studies have reached seemingly contradicting outcomes when using numerical(Miyakawa et al., 2019; Wenk & Huhn, 2013; S. Willett et al., 1993) and analogue(E. Konstantinovskaia, 2005; Mulugeta & Koyi, 1992) approaches to analyze sediment trajectories as a function of changes in erosion, sedimentation, or décollement strength. While some studies showed that the rate and extent of a transition by which sediment trajectories change from generally horizontal to increasingly vertical during accretion change consistently with the initial depth of incoming sediments(Mulugeta & Koyi, 1992; S. Willett, 1992), others predicted different crossover paths for sediments accreting over a range of décollement strengths(E. Konstantinovskaia, 2005). Our models show that both are valid results and that changes in trajectory patterns leading to path crossovers are controlled by the horizontal distance of sediments from the frontal thrust. Starting at a threshold distance from the trench, sediments at different depths follow laminar paths along different trajectories within the wedge. Laminar-type trajectories can be reproduced in a broad range of simulations and are particularly common in models with low sedimentation and décollement strengths. However, the depth dependence of sedimentary paths varies periodically as a function of distance from the trench of specific sedimentary packages (Fig. 3,6). This effect, which is particularly marked in the neighbourhood of the frontal thrust, explains the crossover paths for incoming sedimentary packages at similar depths and different horizontal locations,

as shown by Konstantinovskaia et al. 2005. Therefore, thrust faults in the wedge act as the primary agent controlling whether sediments sustain depth-controlled laminar flow or mix.

The thermal maturity that incoming sediments reach varies periodically as a function of thrust frequency. Although previous research considered non-laminar sediment trajectories as chaotic(Mary et al., 2013), and the wide variety of trajectories shown in our models seem to agree with this (Fig 3, Fig S4), patterns emerge when we correlate the lateral and vertical position of incoming sediments with their eventual thermal maturity. Changes in the depth of the thermal maturity boundary are less frequent and have larger amplitudes with increased décollement strength, and especially, increased sedimentation rates (Fig. 4). The periodicity in the thermal maturity boundary marks the periodic oscillation of the predominant trajectory followed by incoming sediments, i.e., between accretion (low thermal maturity path) and underthrusting (high-thermal maturity path). As a result, it should also strongly correlate with the periodicity observed in the evolution of forearc topography(Menant et al., 2020) and the frequency of thrust formation as such in our models. This is expected, given that thrusts are active over longer mean times, and they thus channel material toward the décollement more efficiently, in wedges with stronger décollement or increased sedimentation. While sediments at internal and higher structural positions of the wedge are translated towards the surface and have a lower thermal maturity, sediments at external and lower structural positions are translated towards the décollement and have a relatively higher maturity. This is a relevant observation, for it typifies the causality of particular sediment grains following a high or low maturity path, a long-standing unanswered question(Miyakawa et al., 2019). We corroborate this observation by analyzing the terminal thermal maturity of sediments across a frontal thrust active at a younger age. For example, by showing the thermal maturity of sediments at ~7.5 Myr across a thrust active at ~4 Myr, as in Fig. 7. Whereas this occurs for all thrusts in the wedge, the frontal thrust is particularly pronounced in partitioning sediments into the high and low maturity paths.

Geothermal information stored in the incoming sediments can only be retrieved if sediments are at appropriate locations with respect to emergent thrusts. We illustrate this using two runs of the same model and tracking an artificial thermal anomaly imposed on incoming sediments at two different locations (Fig. 7). This hypothetical thermal anomaly can be conceptualized as any alteration of the thermal maturity profile of incoming sediments, for example, elevated heat flows by an antecedent magmatic intrusion. While the change in $\%R_0$ associated with the short-lived thermal anomaly results in

abnormally high values of thermal maturity in both sediment packages, it can only be retrieved for the end-model run of sediments located further from the trench (those in the right panel, Fig. 7b). Contrarily, the end-model run of sediments closer to the trench (those in the left panel, Fig. 7a) shows no signs of discontinuity in the thermal maturity distribution of the wedge. This is because we deliberately placed the thermal anomaly at sites that evolve at two structural locations during the model run, i.e., above and below a yet-undeveloped frontal thrust (Fig. 7). The sediment sector affected by the thermal anomaly closer to the trench is overthrusted by the frontal thrust and remains in a footwall location thereafter (Fig. 7a). In contrast, the homologous sedimentary package further away from the trench is accreted by the frontal thrust and remains in a hanging-wall location (Fig. 7b). Thus, the preservation of the record of an antecedent thermal anomaly is only possible in the former case. We further note that, in our simulations, the entire vertical column of sediments records the thermal anomaly, while in nature, the anomaly may affect only sediments at the deeper locations of the sedimentary pile, which are in turn the sediments that most likely to follow a high-maturity path. We thus regard the possibility of retrieving such antecedent geothermal information as minimal.

The main implications of this contribution emerge from its predictive power. Our approach can predict to a precise the thermal maturity of sediments and the uncertainty associated with the maximum exposure temperature in accretionary contexts with known structuration. More accurate quantification of the thermal evolution and thermal state of accreted sediments reduces the uncertainties attached to the location of temperature-led transformations of organic material into hydrocarbons in subduction margins and other accretionary contexts. Such increased accuracy in the distribution of thermally mature sediments may also be applied for improved assessments of the evolution in time of any other geothermal process, including seismic slip, magmatic and metamorphic extent, porosity, compaction and diagenesis of sediments, and the reconstruction of convergent margins in general(Bostick & Pawlewicz, 1984; Ferreiro Mählmann & Le Bayon, 2016; Rabinowitz et al., 2020; A. Sakaguchi et al., 2011; Totten & Blatt, 1993; Underwood et al., 1992).

Finally, among the three methods of $\%R_0$ computation, Easy$\%R_0$ and Basin$\%R_0$ are clearly more consistent and well-constrained on a wide range of thermal maturity in comparison to Simple$\%R_0$, which seems to be particularly useful for a smaller range of thermal maturity values. This simply illustrates the fact that while Easy$\%R_0$ and Basin$\%R_0$ computation deals with several parallel reactions related to the maturity of kerogen(and hence multiple activation energies),

the Simple%R_0 is baked on best-fitted single activation energy, and hence yields large confidence intervals at the extreme %R_0 values. Additionally, the inclusion of the higher activation energy reactions in Basin%R_0 makes it the best-suited formulation for sediments at the deeper and shear zone sediments which usually get saturated using Easy%R_0.

4. Conclusion

This study demonstrates how contractional faults alter the paths of sediments as they accrete and how this fundamentally controls the distribution of the thermal maturity of sediments in accretionary wedges and emphasizes the role that sedimentation rate and interplate contact strength have in such distribution. The increased resolution of our approach leads to findings that have relevant implications. For example, the geothermal history that can be retrieved from the thermal maturity of sediments in drills, i.e., at the shallow wedge, provides, at best, an incomplete record that is skewed towards the thermal evolution of sediments near the trench. Coevally, relevant sectors of sediments located further seaward, when not subducted, follow high-maturity paths that overprint their antecedent thermal history. Finally, this study also provides a first-order uncertainty measure for the thermal maturity of sediments based on the diversity in their trajectory.

References

Arai, R., Kodaira, S., Henrys, S., Bangs, N., Obana, K., Fujie, G., et al. (2020). Three‐dimensional P wave velocity structure of the northern hikurangi margin from the NZ3D experiment: Evidence for fault‐bound anisotropy. *Journal of Geophysical Research, [Solid Earth]*, *125*(12). https://doi.org/10.1029/2020jb020433

Argo. (2022). Argo float data and metadata from Global Data Assembly Centre (Argo GDAC) [Data set]. SEANOE. https://doi.org/10.17882/42182

Bostick, N. H., & Pawlewicz, M. J. (1984). Paleotemperatures based on vitrinite reflectance of shales and limestone in igneous dike aureoles in the Upper Cretaceous Pierre shale, Walsenburg, Colorado. Retrieved from http://archives.datapages.com/data/rmag/SourceRocks84/bostick.pdf

Burg, J.-P., & Gerya, T. V. (2005). The role of viscous heating in Barrovian metamorphism of collisional orogens: thermomechanical models and application to the Lepontine Dome in the Central Alps. *Journal of Metamorphic*

Geology, *23*(2), 75–95.

Burnham, A. K., & Sweeney, J. J. (1989). A chemical kinetic model of vitrinite maturation and reflectance. *Geochimica et Cosmochimica Acta*, *53*(10), 2649–2657.

Byrne, T., & Fisher, D. (1990). Evidence for a weak and overpressured décollement beneath sediment-dominated accretionary prisms. *Journal of Geophysical Research*. https://doi.org/10.1029/jb095ib06p09081

Davis, D., Suppe, J., & Dahlen, F. A. (1983). Mechanics of fold-and- thrust belts and accretionary wedges. *Journal of Geophysical Research*. https://doi.org/10.1029/JB088iB02p01153

Dewing, K., & Sanei, H. (2009). Analysis of large thermal maturity datasets: Examples from the Canadian Arctic Islands. *International Journal of Coal Geology*, *77*(3), 436–448.

Dominguez, S., Malavieille, J., & Lallemand, S. E. (2000). Deformation of accretionary wedges in response to seamount subduction: Insights from sandbox experiments. *Tectonics*, *19*(1), 182–196.

Ferreiro Mählmann, R., & Le Bayon, R. (2016). Vitrinite and vitrinite like solid bitumen reflectance in thermal maturity studies: Correlations from diagenesis to incipient metamorphism in different geodynamic settings. *International Journal of Coal Geology*, *157*, 52–73.

Fillon, C., Huismans, R. S., & van der Beek, P. (2012). Syntectonic sedimentation effects on the growth of fold-and-thrust belts. *Geology*, *41*(1), 83–86.

Fukuchi, R., Yamaguchi, A., Yamamoto, Y., & Ashi, J. (2017). Paleothermal structure of the N ankai inner accretionary wedge estimated from vitrinite reflectance of cuttings. *Geochemistry, Geophysics, Geosystems*, *18*(8), 3185–3196.

Gerya, T. (2019). *Introduction to Numerical Geodynamic Modelling*. Cambridge University Press.

Gerya, T. V., & Yuen, D. A. (2003). Characteristics-based marker-in-cell method with conservative finite-differences schemes for modeling geological flows with strongly variable transport properties. *Physics of the Earth and Planetary Interiors*, *140*(4), 293–318.

Giunchi, C., & Ricard, Y. (1999). High-pressure/low-temperature metamorphism and the dynamics of an accretionary wedge. *Geophysical Journal International*, *136*(3), 620–628.

Górszczyk, A., Operto, S., Schenini, L., & Yamada, Y. (2019). Crustal-scale depth imaging via joint full-waveform inversion of ocean-bottom seismometer data and pre-stack depth migration of multichannel seismic data: a case study from the

eastern Nankai Trough. *Solid Earth*, *10*(3), 765–784.

Hori, T., & Sakaguchi, H. (2011). Mechanism of décollement formation in subduction zones. *Geophysical Journal International*, *187*(3), 1089–1100.

Konstantinovskaia, E. (2005). Erosion and exhumation in accretionary orogens: Experimental and geological approaches. *Geochemistry, Geophysics, Geosystems*. Retrieved from https://agupubs.onlinelibrary.wiley.com/doi/abs/10.1029/2004GC000794

Konstantinovskaia, E., & Malavieille, J. (2005). Erosion and exhumation in accretionary orogens: Experimental and geological approaches. *Geochemistry, Geophysics, Geosystems*. https://doi.org/10.1029/2004gc000794

Korup, O., Hayakawa, Y., Codilean, A. T., Matsushi, Y., Saito, H., Oguchi, T., & Matsuzaki, H. (2014). Japan's sediment flux to the Pacific Ocean revisited. *Earth-Science Reviews*, *135*, 1–16.

Luján, M., Rossetti, F., Storti, F., Ranalli, G., & A. Socquet. (2010). Flow trajectories in analogue viscous orogenic wedges: Insights on natural orogens. *Tectonophysics*, *484*(1), 119–126.

Malavieille, J., & Trullenque, G. (2009). Consequences of continental subduction on forearc basin and accretionary wedge deformation in SE Taiwan: Insights from analogue modeling. *Tectonophysics*, *466*(3), 377–394.

Mannu, U., Ueda, K., Willett, S. D., Gerya, T. V., & Strasser, M. (2016). Impact of sedimentation on evolution of accretionary wedges: Insights from high-resolution thermomechanical modeling. *Tectonics*. https://doi.org/10.1002/2016tc004239

Mannu, U., Ueda, K., Willett, S. D., Gerya, T. V., & Strasser, M. (2017). Stratigraphic signatures of forearc basin formation mechanisms. *Geochemistry, Geophysics, Geosystems*, *18*(6), 2388–2410.

Mary, B. C. L., Maillot, B., & Leroy, Y. M. (2013). Deterministic chaos in frictional wedges revealed by convergence analysis. *International Journal for Numerical and Analytical Methods in Geomechanics*. https://doi.org/10.1002/nag.2177

Menant, A., Angiboust, S., Gerya, T., Lacassin, R., Simoes, M., & Grandin, R. (2020). Transient stripping of subducting slabs controls periodic forearc uplift. *Nature Communications*, *11*(1), 1823.

Miyakawa, A., Kinoshita, M., Hamada, Y., & Otsubo, M. (2019). Thermal maturity structures in an accretionary wedge by a numerical simulation. *Progress in Earth and Planetary Science*, *6*(1), 8.

Mugnier, J. L., Baby, P., Colletta, B., Vinour, P., Bale, P., & Leturmy, P. (1997). Thrust geometry controlled by erosion and sedimentation: A view from analogue models. *Geology*, *25*(5), 427–430.

Mulugeta, G., & Koyi, H. (1992). Episodic accretion and strain partitioning in a model sand wedge. *Tectonophysics*, *202*(2), 319–333.

Nakanishi, A., Takahashi, N., Yamamoto, Y., Takahashi, T., Citak, S. O., Nakamura, T., et al. (2018). Three-dimensional plate geometry and P-wave velocity models of the subduction zone in SW Japan: Implications for seismogenesis. *Geology and Tectonics of Subduction Zones: A Tribute to Gaku Kimura: Geological Society of America Special Paper*, *534*, 69–86.

Ohmori, K., Taira, A., Tokuyama, H., Sakaguchi, A., Okamura, M., & Aihara, A. (1997). Paleothermal structure of the Shimanto accretionary prism, Shikoku, Japan: Role of an out-of-sequence thrust. *Geology*, *25*(4), 327–330.

Platt, J. P. (1986). Dynamics of orogenic wedges and the uplift of high-pressure metamorphic rocks. *GSA Bulletin*, *97*(9), 1037–1053.

Platt, J. P. (1993). Exhumation of high-pressure rocks: a review of concepts and processes. *Terra Nova*, *5*(2), 119–133.

Quigley, T. M., & Mackenzie, A. S. (1988). The temperatures of oil and gas formation in the sub-surface. *Nature*, *333*(6173), 549–552.

Rabinowitz, H. S., Savage, H. M., Polissar, P. J., Rowe, C. D., & Kirkpatrick, J. D. (2020). Earthquake slip surfaces identified by biomarker thermal maturity within the 2011 Tohoku-Oki earthquake fault zone. *Nature Communications*, *11*(1), 533.

Ranalli, G. (1995). *Rheology of the Earth*. Springer Science & Business Media.

Ruh, J. B. (2017). Effect of fluid pressure distribution on the structural evolution of accretionary wedges. *Terra Nova*, *29*(3), 202–210.

Ruh, J. B. (2020a). Numerical modeling of tectonic underplating in accretionary wedge systems. *Geosphere*, *16*(6), 1385–1407.

Ruh, J. B. (2020b). Numerical modelling of tectonic underplating in accretionary wedges (p. 5607).

Sakaguchi, A., Yanagihara, A., Ujiie, K., Tanaka, H., & Kameyama, M. (2007). Thermal maturity of a fold–thrust belt based on vitrinite reflectance analysis in the Western Foothills complex, western Taiwan. *Tectonophysics*, *443*(3), 220–232.

Sakaguchi, A., Chester, F., Curewitz, D., Fabbri, O., Goldsby, D., Kimura, G., et al. (2011). Seismic slip propagation to the updip end of plate boundary subduction interface faults: Vitrinite reflectance geothermometry on Integrated Ocean Drilling Program NanTro SEIZE cores. *Geology*. https://doi.org/10.1130/g31642.1

Schmoker, J. W., & Gautier, D. L. (1988). Sandstone porosity as a function of thermal maturity. *Geology*, *16*(11), 1007–1010.

Simpson, G. D. H. (2010). Formation of accretionary prisms influenced by sediment subduction and supplied by sediments from adjacent continents. *Geology*, *38*(2), 131–134.

Storti, F., & Mcclay, K. (1995). Influence of syntectonic sedimentation on thrust wedges in analogue models. https://doi.org/10.1130/0091-7613(1995)023<0999

Sugihara, T., Kinoshita, M., Araki, E., Kimura, T., Kyo, M., Namba, Y., et al. (2014). Re-evaluation of temperature at the updip limit of locked portion of Nankai megasplay inferred from IODP Site C0002 temperature observatory. *Earth, Planets and Space*. https://doi.org/10.1186/1880-5981-66-107

Tesei, T., Lacroix, B., & Collettini, C. (2015). Fault strength in thin-skinned tectonic wedges across the smectite-illite transition: Constraints from friction experiments and critical tapers. *Geology*, *43*(10), 923–926.

Tissot, B. P., & Welte, D. H. (2013). *Petroleum Formation and Occurrence*. Springer Science & Business Media.

Tissot, B. P., Pelet, R., & Ungerer, P. H. (1987). Thermal History of Sedimentary Basins, Maturation Indices, and Kinetics of Oil and Gas Generation. *AAPG Bulletin*, *71*(12), 1445–1466.

Tobin, H., Hirose, T., Saffer, D., Toczko, S., Maeda, L., Kubo, Y., et al. (2015). Site C0002. *Proceedings of the IODP*. https://doi.org/10.2204/iodp.proc.348.103.2015

Tobin, H. J., & Saffer, D. M. (2009). Elevated fluid pressure and extreme mechanical weakness of a plate boundary thrust, Nankai Trough subduction zone. *Geology*, *37*(8), 679–682.

Totten, M. W., & Blatt, H. (1993). Alterations in the non-clay-mineral fraction of pelitic rocks across the diagenetic to low-grade metamorphic transition, Ouachita Mountains, Oklahoma and Arkansas. *Journal of Sedimentary Research*, *63*(5), 899–908.

Underwood, M. B., Laughland, M. M., Byrne, T., Hibbard, J. P., & DiTullio, L. (1992). Thermal evolution of the Tertiary Shimanto Belt, Muroto Peninsula, Shikoku, Japan. *The Island Arc*. https://doi.org/10.1111/j.1440-1738.1992.tb00064.x

Wang, K., & He, J. (1999). Mechanics of low-stress forearcs: Nankai and Cascadia. *Journal of Geophysical Research, [Solid Earth]*, *104*(B7), 15191–15205.

Waples, D. W. (1981). *Organic Geochemistry for Exploration Geologists*. Springer Netherlands.

Wenk, L., & Huhn, K. (2013). The influence of an embedded viscoelastic–plastic layer on kinematics and mass transport pattern within accretionary wedges. *Tectonophysics*, *608*, 653–666.

Willett, S. (1992). Dynamic and kinematic growth and change of a Coulomb wedge. *McClay, K. R.*, 19–31.

Willett, S., Beaumont, C., & Fullsack, P. (1993). Mechanical model for the tectonics of doubly vergent compressional orogens. *Geology*. https://doi.org/10.1130/0091-7613(1993)021<0371:MMFTTO>2.3.CO

Willett, S. D. (1999). Orogeny and orography: The effects of erosion on the structure of mountain belts. *Journal of Geophysical Research*, *104*, 28957.

Yamamoto, Y., Hamada, Y., Kamiya, N., Ojima, T., Chiyonobu, S., & Saito, S. (2017). Geothermal structure of the Miura–Boso plate subduction margin, central Japan. *Tectonophysics*, *710-711*, 81–87.

List of Tables

Table 1: Properties for the different materials used for the model runs

Rock Type	Density (kg/m^3)	Cohesion (MPa)	Coefficient of friction(μ)	Thermal Conductivity (W/(m K))	Flow law	E (kJ/mol)	n
Water	1000	0	0	20		0	0
Air (Sticky-air)	0	0	0	20		0	0
Décollement	2600	0.001	0.03 /0.08	(1.5+807/(T+77))* (1-exp(-Z^2/1.3e7))	Wet quartzite	154	2.3
Sediments1	2600	0.5/0.05*	4.64/0.2*	(0.96+807/(T+77))* (1-exp(-Z^2/1.3e7))	Wet quartzite	154	2.3
Sediments2	2600	0.5/0.05*	4.64/0.2*	(0.96+807/(T+77))* (1-exp(-Z^2/1.3e7))	Wet quartzite	154	2.3
Upper Continental Crust	2700	1	0.6	0.64+807/(T+77)	Wet quartzite	300	2.3
Lower Continental Crust	2800	1	0.6	0.64+807/(T+77)	Wet quartzite	300	3.2
Upper Oceanic Crust	3000	1	0.6	1.18+474/(T+77)	Plagioclase An75	300	2.3
Lower Oceanic Crust	3000	1	0.6	1.18+474/(T+77)	Plagioclase An75	300	3.2
Mantle Lithosphere	3300	1	0.6	0.73+1293/(T+77)	Dry olivine	532	3.5
Asthenosphere	3300	1	0.6	0.73+1293/(T+77)	Dry olivine	532	3.5

**Strain-softened Cohesion/Coefficient of friction*
T is Temperature, Z is the depth from the seafloor.

Table 2: Model runs and their specific characteristic observations

Models	φ_b	φ / φ_{ss}	*SR*	*L*	α	*D*	$<R_o\%>$	$\%_{top\text{-}half}$	$\%_{Bottom\text{-}half}$
M_0^2	**2°**	**30°/15°**	**None**	**123.2±15.7**	**4.3±0.3°**	**15.5±7.0**	**0.54**	**0.0**	**12.7**
M_0^7	**7°**	**30°/15°**	**None**	**97.7±9.9**	**6.5±0.5°**	**12.1±3.6**	**0.60**	**0.0**	**22.5**
M_0^{12}	**12°**	**30°/15°**	**None**	**77.8±4.8**	**8.9±0.5°**	**8.7±2.1**	**0.67**	**0.0**	**31.3**
$M_{0.1}^{12}$	**12°**	**30°/15°**	**0.1**	**76.1±5.9**	**8.9±0.9°**	**7.3±1.1**	**0.71**	**0.1**	**35.3**
$M_{0.3}^{12}$	**12°**	**30°/15°**	**0.3**	**79.3±8.2**	**8.6±1.3°**	**7.8±2.5**	**0.69**	**0.1**	**32.0**
$M_{0.5}^{12}$	**12°**	**30°/15°**	**0.5**	**79.9±7.4**	**8.5±0.6°**	**9.5±4.0**	**0.71**	**2.7**	**34.4**
$M_{0.7}^{12}$	**12°**	**30°/15°**	**0.7**	**81.3±10.5**	**8.5±1.0°**	**9.9±5.0**	**0.73**	**4.2**	**41.5**
$M_{0.9}^{12}$	**12°**	**30°/15°**	**0.9**	**82.5±11.0**	**8.8±1.5°**	**13.8±7.8**	**0.75**	**14.6**	**51.8**
M_0^{17}	**17°**	**30°/15°**	**None**	**71.6±5.0**	**10.7±0.8°**	**8.8±3.3**	**0.83**	**1.2**	**40.6**
M_0^{22}	**22°**	**30°/15°**	**None**	**62.7±6.0**	**12.8±1.2°**	**8.0±1.8**	**0.94**	**2.0**	**54.0**

φ_b is décollement Strength (internal angle of friction)
φ Sediment Strength
φ_{ss} Sediment Strength (Strain weakened)/(internal angle of friction)
SR Average Sediment rate (mm/yr)
L Average Length (in km) between ~2.5-7.5Myr
α Average Taper angle α (in degrees) between ~2.5-7.5Myr
D Average Distance between the first and second frontal thrust between ~2.5-7.5Myr(in km)
T Average time a frontal thrust remains active between ~3.5-7.5Myr
$<R_o\%>$ Average vitrinite reflectance of the wedge between ~3.5-7.5 Myr
$\%_{top}$ Proportion of >1 eventual ***R_o% (vitrinite reflectance at 7.5 Myr)*** at shallow half of the incoming sediment at 2.5 Myr.
$\%_{bottom}$ Proportion of >1 eventual ***R_o% (vitrinite reflectance at 7.5 Myr)*** at deep half of the concoming sediments.

List of Figures

Fig. 1: *Distribution of thermal maturity for different models at ~7.5 Myr(5 Myr of thermal maturation). Panels A1-A5 show the thermal maturity distribution(computed using Easy%R_0) in subduction wedges of models as a function of décollement strength* $M_0^2 - M_0^{22}$*, respectively. A6-A10 show the thermal maturity distribution in subduction wedges of models function of sedimentation rae* $M_{0.1}^{12} - M_{0.9}^{12}$ *, respectively. The grey color of the markers indicate that no thermal maturity change in these sediments have not occurred. B1-B10 and C1-C10 similarly show the thermal maturity distribution in subduction wedges computed using Simple%R_0 and Basin%R_0 , respectively.*

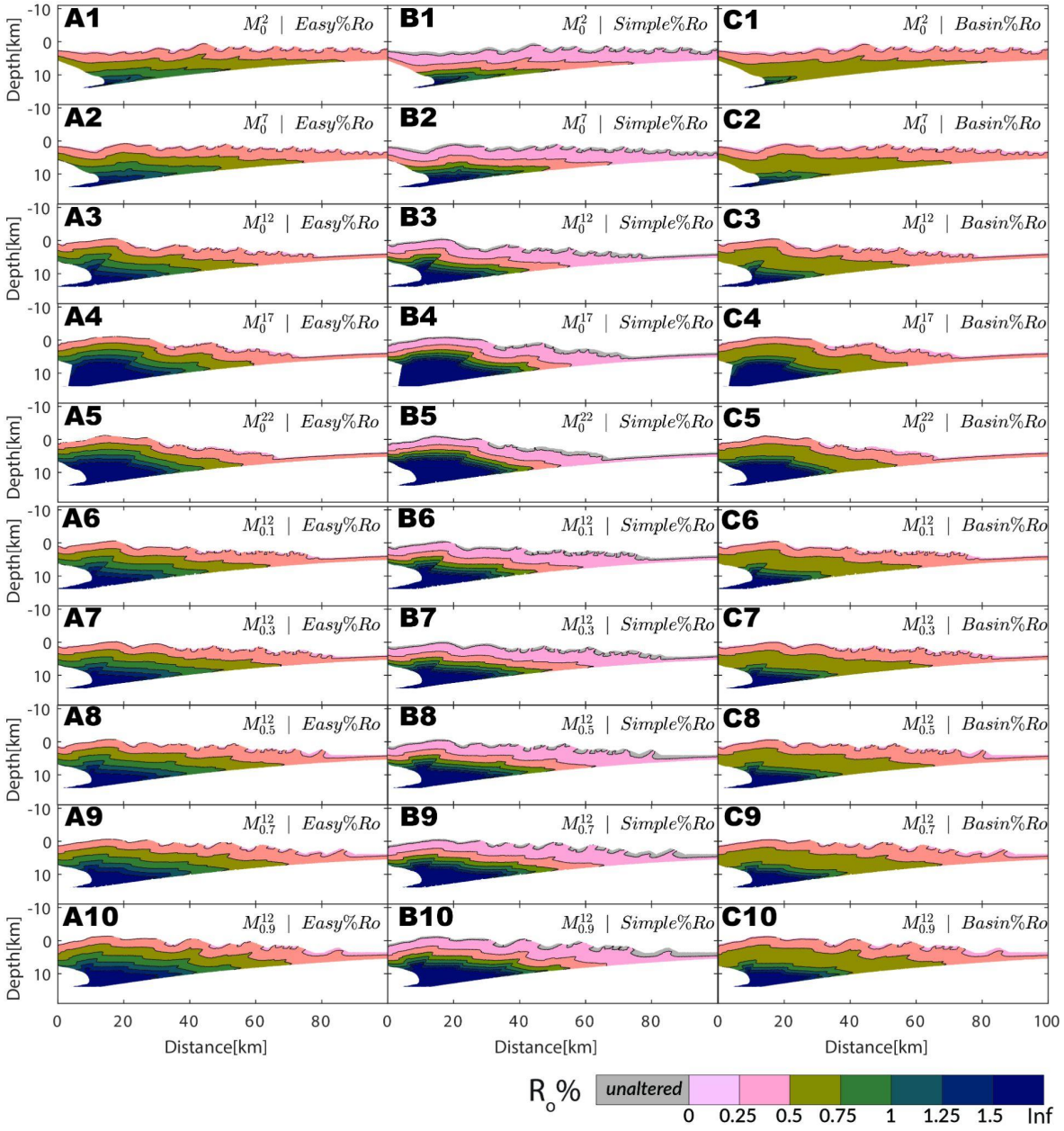

Fig. 2: *The variation of $\%R_0$ for an horizon at the trench depth of each model at 7.5 Myr. Panel A shows all the models with different decollement strench (M_0^2-M_0^{22}). Panel B shows all the models with different sedimentation rates ($M_{0.1}^{12}$-$M_{0.9}^{12}$)*

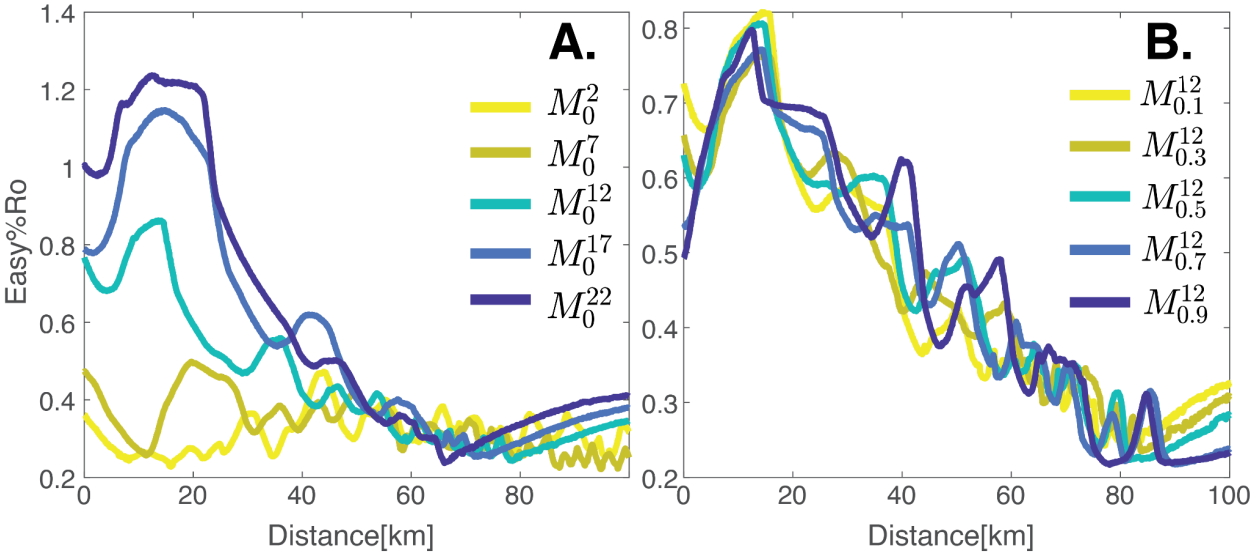

Fig. 3: *Map of thermal maturity at 7.5 Myr mapped to sediments at 2.5 Myr. Panel A1-A5,B1-B5 show the mapping for models* M_0^2-M_0^{22} *and* $M_{0.1}^{12}$-$M_{0.9}^{12}$ *respectively. The vertical axis (distance from the oceanic plate) has been corrected for the bending of the plate. The horizontal axis represents the distance of sediments from the trench. The grey colour of the markers indicates that these sediments have been eroded/reworked due to slope failure. The broken black line represents the mean %R_0 attained sediment at a given distance from the trench. λ represents the horizontal periodicity in mean %R_0 for the given model.*

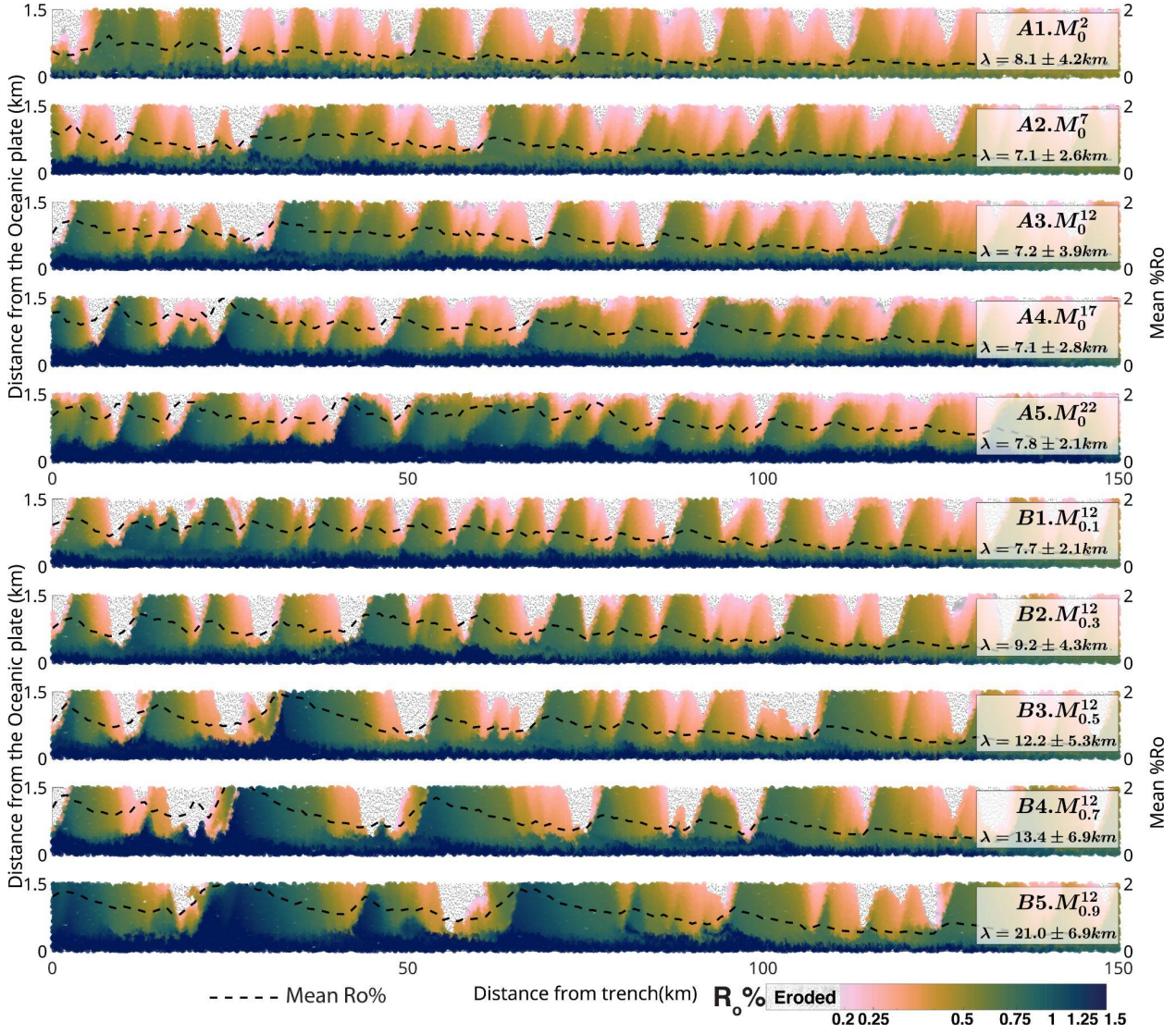

Fig: 4 A. *Vitrinite Reflectance(**R_0%**) vs Maximum Exposure temperature in all models* ***B.*** *Range of 95% CI for Easy%Ro, Simple%Ro and Basin%Ro*

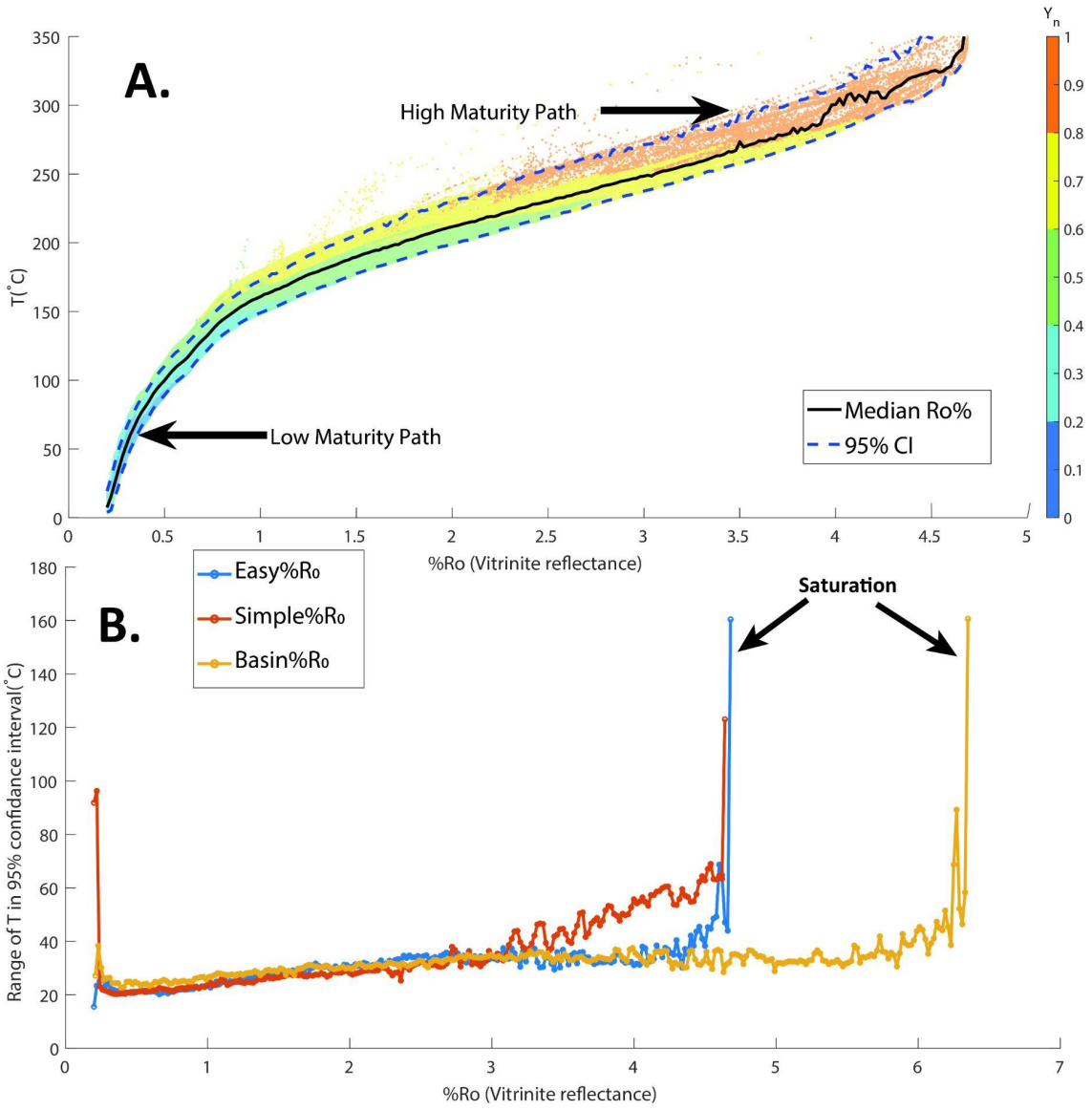

Fig.5: *Depth vs Thermal maturity(%R_0). The shaded (in voilet) region shows the range of observed R_o%(mean±1SD) from the C0002 borehole (Fukuchi et al., 2017),colored lines represent the values in models* $M_0^{12}, M_{0.1}^{12}, M_{0.3}^{12}, M_{0.5}^{12}, M_{0.7}^{12}, M_{0.9}^{12}$

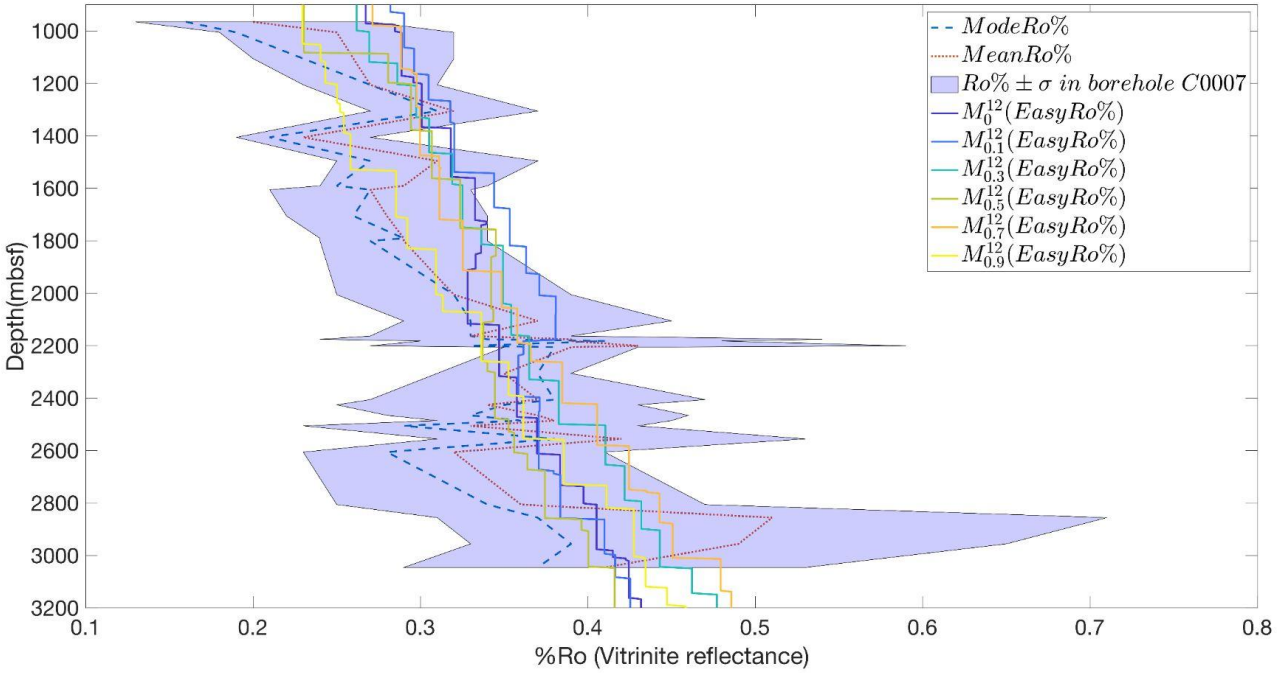

. .

Fig. 6: *Panel A Mapping of eventual thermal maturity(vitrinite reflectance at 7.5Myr) to a frontal thrust at ~4Myr in model* $M_{0.9}^{12}$*. The lithology of the wedge is shown in panel B. The half arrow represents the active frontal thrust.*

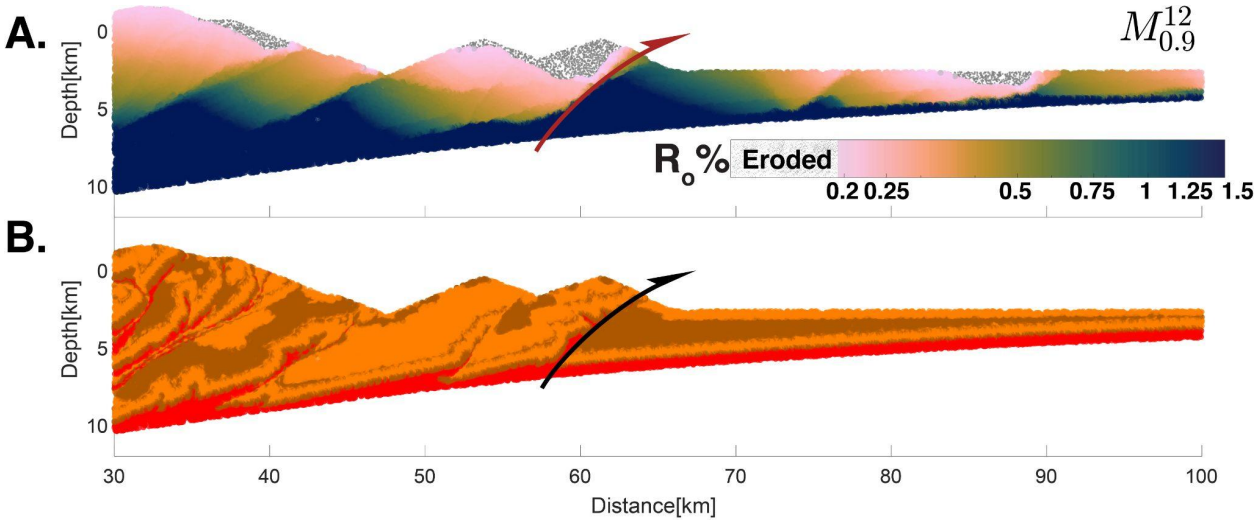

Fig. 7: *Position dependency of thermal maturity preservation. Panel* ***A.*** *Model state at ~2.5 Myr with a thermal anomaly placed at 110-125 km from backstop* ***B.*** *Model state at ~2.5 Myr with a thermal anomaly placed at 140-155 km from the backstop.* ***C.*** *Model state at ~7.5 Myr.*

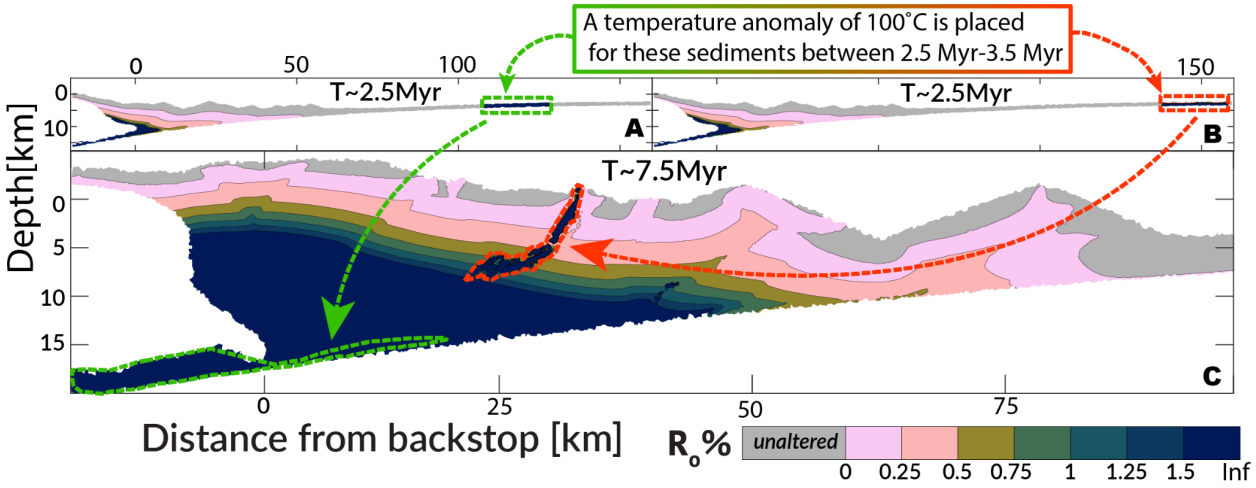

Supplementary material for Thrusts control the thermal maturity of accreted sediments

Utsav Mannu[1,*], David Fernández-Blanco[2], Ayumu Miyakawa[3], Taras Gerya[4], and Masataka Kinoshita[5]

[1]Discipline of Earth Sciences, Indian Institute of Technology, Gandhinagar, India

[2] Barcelona Center of Subsurface Imaging, Institut de Ciències del Mar (ICM-CSIC), Barcelona, Spain;

[3]Geological Survey of Japan, AIST

[4]Institute of Geophysics, ETH Zurich

[5]Earthquake Research Institute, UTokyo

Correspondence to: Utsav Mannu (utsav.mannu@iitgn.ac.in)

Contents

Supplementary text

In our visco-plastic/brittle model with variable viscosity, finite conservative difference ensures conservation of stresses by harmonizing the formulation of deviatoric stress across adjacent nodes. The topographic boundary in the model is simulated by an adaptive irregular surface grid coupled to the thermomechanical grid. The surface processes applied to the model are primarily implemented on this grid and are realized through the conversion of rock markers to air/water markers across this boundary, and vice-versa. Surface grid nodes can also be advected horizontally and vertically using velocities interpolated from the thermomechanical grid. As a result, both tectonic forcing and surface processes can change the model topography. Most of the sedimentation in the model happens as a cascading deposition of sediments from sea to land in subsequent basins. A free-slip boundary condition is implemented on all boundaries, except for the lower one which remains permeable to ensure mass conservation. We set thermally insulating boundary conditions on all sides except the lower one where the external thermal boundary condition is implemented.

1. Governing equations

The mass conservation is described by the continuity equation with the Boussinesq approximation of incompressibility as:

$$\frac{\partial v_x}{\partial x} + \frac{\partial v_y}{\partial y} = 0 \qquad (eq.1)$$

The equation for conservation of momentum with an incompressibility assumption is expressed in the 2D- stokes equation, for the *x*-axis and *y*-axis, respectively, as follows:

$$\frac{\partial \sigma_{xx}}{\partial x} + \frac{\partial \sigma_{xy}}{\partial y} = \frac{\partial P}{\partial x} \qquad (eq.2)$$

$$\frac{\partial \sigma_{yy}}{\partial y} + \frac{\partial \sigma_{xy}}{\partial x} = \frac{\partial P}{\partial x} - g\rho(T, P, C, M) \qquad (eq.3)$$

Where density $g\rho(T, P, C, M)$ depends on temperature (*T*), pressure (*P*), composition (*C*), and mineralogy (*M*).

The thermal equation used in the model is as follows:

$$\rho C_P \frac{DT}{Dt} = -\frac{\partial q_x}{\partial x} - \frac{\partial q_y}{\partial y} + H_r + H_a + H_s + H_l \qquad (eq.4)$$

where,

$$q_x = -k(T,C)\frac{\partial T}{\partial x}, q_y = -k(T,C)\frac{\partial T}{\partial y} \qquad (eq.5)$$

$$H_a = T\alpha\frac{DP}{Dt}, H_s = \sigma_{xx}\dot{\varepsilon}_{xx} + \sigma_{yy}\dot{\varepsilon}_{yy} + \sigma_{xx}\dot{\varepsilon}_{xy} \qquad (eq.6)$$

Where $D/DT$is a lagrangian time derivative, and x and y denote the horizontal and vertical coordinates, respectively; $\sigma_{xx}, \sigma_{xy}, \sigma_{yy}$ are components of the deviatoric stress tensor; $\dot{\varepsilon}_{xx}, \dot{\varepsilon}_{yy}, \dot{\varepsilon}_{xy}$ are components of the strain rate tensor; P is pressure; T is temperature; $q_x$and q_y are the components of heat flux in the horizontal and vertical direction; ρ is density; $g$is the gravitational acceleration; $C_p$is the isobaric heat capacity; H_r, H_a, H_s, H_l denote, the radioactive, adiabatic, shear and latent heat production, respectively. $k(T,C)$ is the thermal conductivity, a function of composition, depth, and temperature(Table 1). To match the empirical relationship between depth and thermal conductivity, as measured on core samples in the borehole at IODP Site C0002(Sugihara et al., 2014; H. Tobin et al., 2015). To simulate the decrease in thermal conductivity near the surface caused by increased porosity, we modify the thermal conductivity formulation for sediments as a function of temperature and depth as follows

$$k_{sed} = 0.96 + \frac{807}{T+77}(1 - e^{\frac{-Z^2}{1.3e^7}})$$

For décollement we again use a similar relationship however with a larger thermal conductivity near the surface to emulate higher heat transfer in shear zones due to fluid advection

$$k_{sed} = 1.5 + \frac{807}{T+77}(1 - e^{\frac{-Z^2}{1.3e^7}})$$

2. Rheological model

The expression for effective creep viscosities(η_{eff}) of the materials used in the model is determined from experimental data(Ranalli, 1995) using a calibrated parameterized function of pressure(*P*) and temperature(*T*), known as flow law (Table 1).

$$\eta_{eff} = F(\dot{\varepsilon}_{II})^{1-n} A_D{}^{\frac{-1}{n}} h^m exp\left(-\frac{E_a + V_a P}{nRT}\right) \qquad (eq.7)$$

where, *F* is a dimensionless constant that depends on the type of experiments used for calibration, *P* is pressure (Pa), *T* is the temperature (K), *R* is the gas constant (8.314 J/K/mol), h is grain size (m) and A_D, n, m, E_a and V_a are experimentally determined rheological parameters: A_D is the material constant ($Pa^{-n}s^{-1}m^{-m}$), n is the stress exponent, m is the grain size exponent, E_a is activation energy (J/mol) and V_a is activation volume (J/Pa). As dislocation creep does not depend on grain size therefore we assume $h^m = 1$. $\dot{\varepsilon}_{II}$ is the second invariant of strain tensor computed as

$$\dot{\varepsilon}_{II} = \sqrt{\frac{\dot{\varepsilon}_{ij} * \dot{\varepsilon}_{ij}}{2}} \qquad (eq.8)$$

The model uses visco-plastic rheology to account for both brittle rheology of the shallower and colder rigid lithosphere and deeper, hotter ductile lithosphere and asthenosphere. Using the Mohr-Coulomb failure criterion we limit effective viscosity as

$$\eta_{eff} \leq \frac{c + Psin(\varphi)}{2\dot{\varepsilon}_{II}} \qquad (eq.9)$$

Where, c is cohesion and φ is an effective internal angle of friction or $\mu = tan(\varphi)$ where μis the coefficient of internal friction.

3. Boundary conditions

A free-slip boundary condition is implemented on all boundaries, except on the lower boundary, where is passable in the vertical direction. Where we implement, an external free slip condition similar to (Burg & Gerya, 2005) where a free slip condition is satisfied at an external boundary such that

$$\frac{\partial V_x}{\partial x} = 0, \frac{\partial V_y}{\partial y} = \frac{V_y}{\Delta Y_{external}} \qquad (eq.16)$$

Where, V_x and V_y, are the velocities in the horizontal and vertical directions at the boundary, $\Delta Y_{external}$ is the depth that lies outside the modeling domain, and where free slip condition is maintained. Similarly, we set thermally insulating boundary conditions on all sides except the lower one where the external thermal boundary condition is implemented.

4. Surface processes

The rock-water/air boundary is simulated by an adaptive irregular grid that is advected horizontally and vertically and is coupled to the thermomechanical grid which controls the tectonic change of the surface. Apart from the tectonic changes, surface processes prescribed in the model can also change the topography. The surface process in the model is controlled by conversion of rock markers to air/water and vice versa. All sedimentation in the model happens as a focused deposition of sediments from sea to land in morphological depressions (e.g. trench) is modelled as follows (Figure S2)

$$Y_{new} = Y_{old} + K \bullet Y_{fill} \qquad (eq.10)$$

Where, $K = min\left(\frac{V_{budget}}{V_{basin}}, 1\right)$

Due to the arbitrary shape of the basin, filling the basin using the above equation can overfill /underfill in a specific step. However, we compute the volume of the sediments that have been deposited and balance out the sediment deficit/overfill in the next step. Therefore over long run the sedimentation amount remains equivalent to the prescribed amount.

5. Limitations

For instance, even with a minimum grid size of 150 m x 500 m, the model is not able to simulate very narrow faults that usually occur in nature and lead to a very local increase in thermal maturity. Therefore, while the thermal maturity anomaly observed in the borehole can be concentrated at the site of the fault which can be only a few centimeters wide, thermal maturity for our model can be spread over several hundred meters (Fig. 7). Wider faults also result in a smaller characteristic time for local heat diffusion, meaning the rise in temperature due to viscous heating in faults is sustained for a smaller period. Consequently, in our models, the relative rise in thermal maturity of sediments in faults is far less compared to the observations in the borehole. This problem could be resolved in the future using adaptive gridding, where one can temporarily increase the resolution in zones with high strain rates, leading to much narrower faults and concentrated elevation of heat and maturity in faults.

Another assumption in our model is that the model does not contain compaction or an increase in sediment strength with increasing depth and thickness of the wedge. Although this was done to keep the model simple, in the future one can introduce an empirical increase in material strength both with depth and seaward to landward. Additionally, thermal maturity which is related to porosity by (Schmoker & Gautier, 1988) can also be used to give a measure of compaction in the wedge and could be linked to material strength. However, one needs to be careful while implementing this relationship as fault zones which generally have a higher thermal maturity due to viscous heating tend to have lower strength. We have also not considered the influence of fluid flow in our models, which can have a significant impact on the maturity value, especially in the fault zones. However, to mimic this effect we used elevated values of conductivity for the weak material present in the décollement.

6. Initial model setup

The modelling domain is 3500 km wide and 350 km deep and is discretized into 1284 × 401 nodes populated with ~25 million markers. At the site of accretionary wedge evolution, we assign a significantly higher resolution of 130 m (vertical) × 300 m (horizontal), which steadily decreases near the boundary of the modelling domain. The simulation consists of an oceanic plate converging with a velocity of ~5 cm/yr and subducting beneath the continental plate (see Fig. S1). The oceanic

plate consists of a 1-km-thick upper oceanic crust and a 7-km-thick lower oceanic crust underlain by a 47-km-thick mantle lithosphere. We use a thin (10 km) "sticky air" layer to overlay the top face of the rock strata inside the model which is a fluid with a low viscosity of 5E+17 Pa.s. and a low density, similar to air (white in Figure S1) or water (light blue in Figure S1). Displacement along the megathrust, at the contact between subducting oceanic plate and the overriding continental plate, occurs in a relatively weak basal layer in accretionary wedges across the globe(Byrne & Fisher, 1990). We simulate this with a predefined configuration at the interplate, with a 350-meter-thick décollement below a 1km thick sediment layer. The wedge forms above this interphase by accretion of sediments against the continental plate. The continental plate consists of an upper and lower continental crust with thicknesses of~ 20 km and ~15 km, respectively, and underlain by a mantle lithosphere of ~25 km. The transition between the lithosphere and asthenosphere is prescribed to occur at 1300℃. A weak layer is emplaced at the junction of both plates, which fails mechanically and leads to subduction initiation. Please refer to Table 1 for the rheological and thermal properties of all the materials used.

List of supplementary figures.

Fig. S1:*Initial model setup.* ***A.*** *The lithological and geothermal map of the whole computational domain with boundary conditions.* ***B.*** *The zoomed lithological and geothermal map of the inset illustrates the junction of continental and oceanic plates. The colors represent different lithology of the materials used in the models, with upper and lower crust represented by light and dark grey, upper and lower oceanic crust represented by dark and light green. The arrows around the computational domain represent the imposed boundary conditions, while the white contour lines(dashed in the zoomed panel) show the geothermal gradients used for the initial model. The numbers on the white contour lines represent the temperature values in ℃ for the contour.*

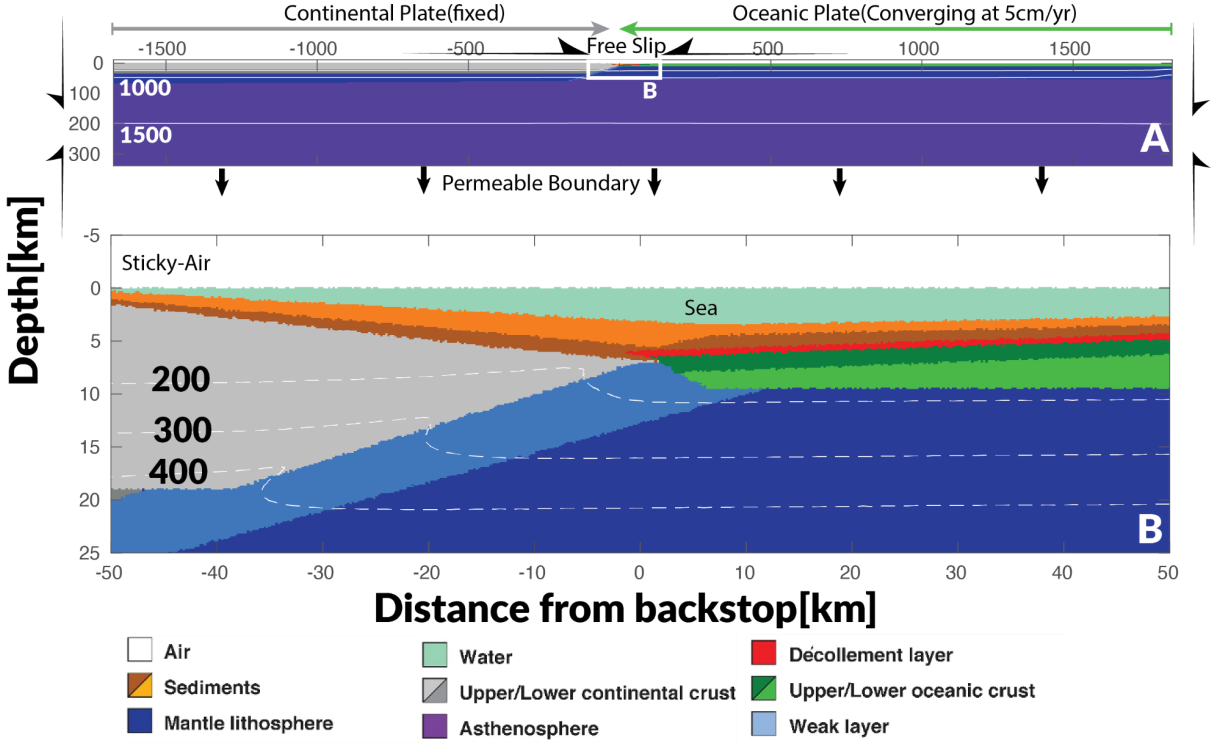

Fig S2: *Scheme of trench sedimentation in models (taken from (Mannu et al., 2017))*

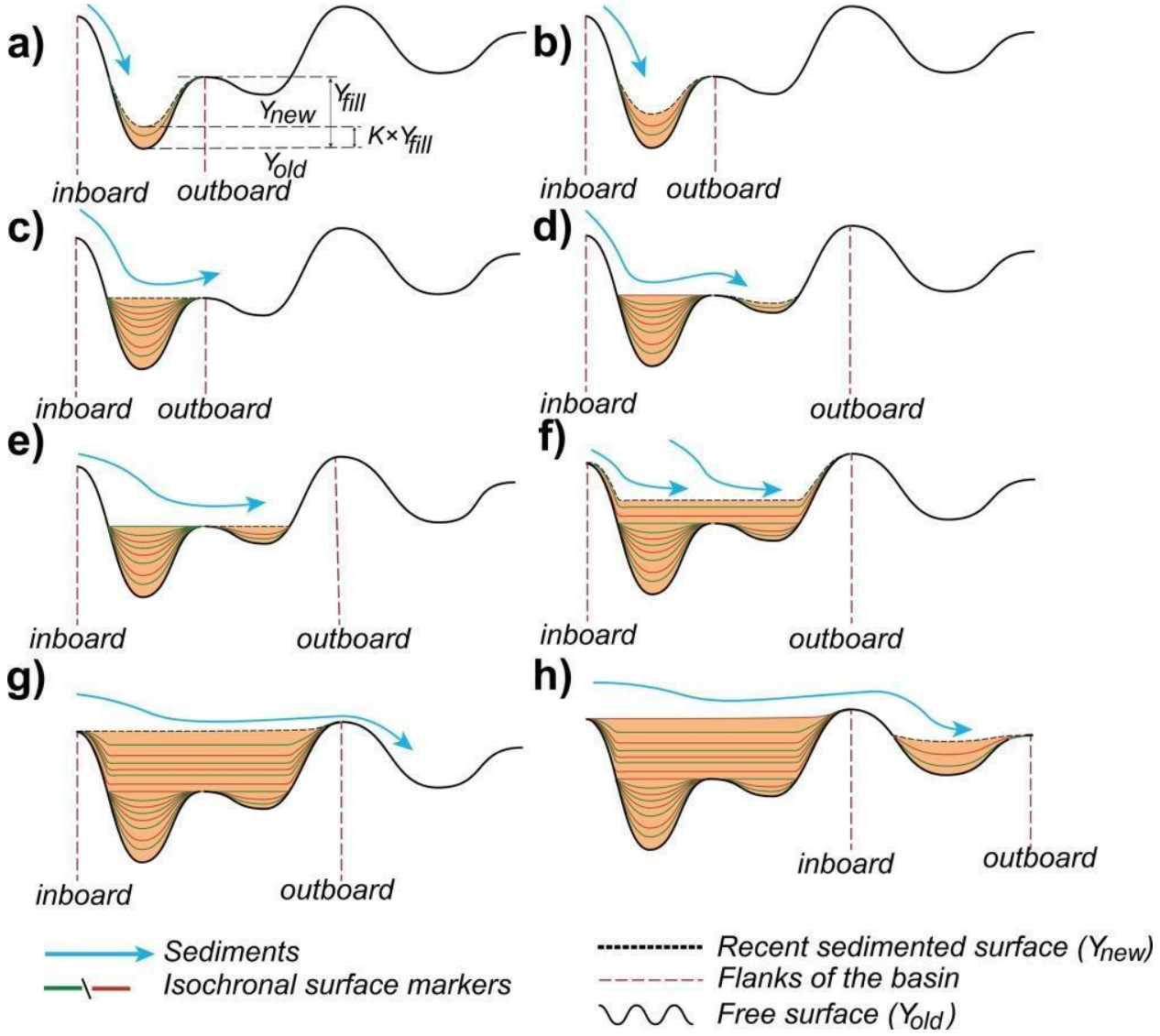

Fig. S3: *Plot of Temperature vs Depth profile in for water-sediment interaction using the data from the International Argo Program and the national programs that contribute for the location(represented by the white square) given in the inset. The magenta circle represent the Temperature vs Depth profile from the data while the black line is the fitted thermocline used in our models for water-sediment thermal interaction.*

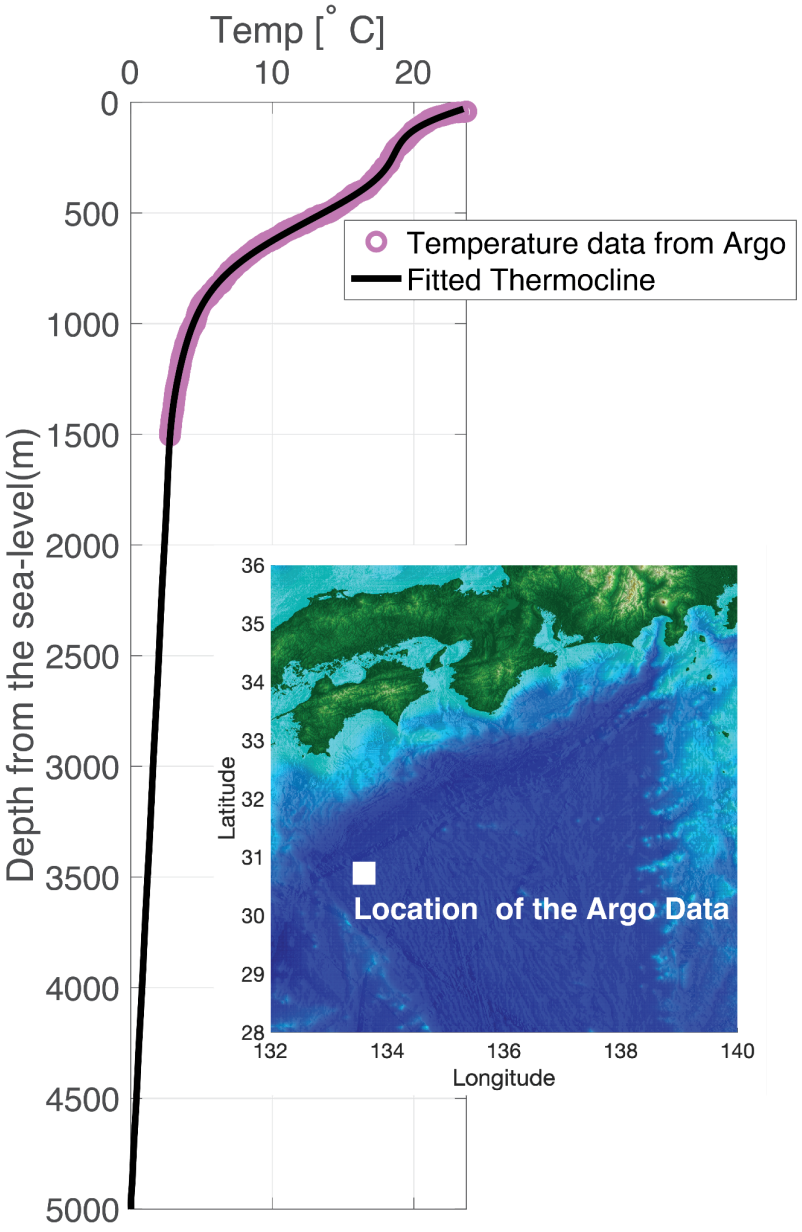

Fig. S4: *Plot of Temperature vs Depth profile in all models compared to Temperature-depth profile based on in-situ temperature from the long-term borehole monitoring system (indicated red patch is the range of temperature estimated by (Sugihara et al., 2014))*

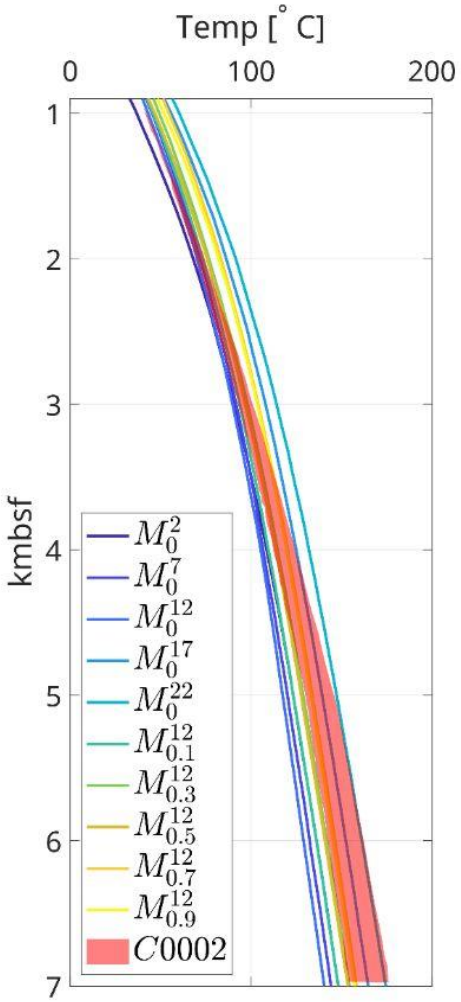

Fig. S5 *Trajectory of sediments in model . The wedge on top shows the location of individual boreholes relative to the position of the trench at 2.5 Myr. In each borehole, A-L 10 points are plotted for their trajectories between 2.5 Myr and 7.5 Myr. The color of markers in the trajectories represent the evolution of thermal maturity on individual sediment markers while undergoing evolution.*

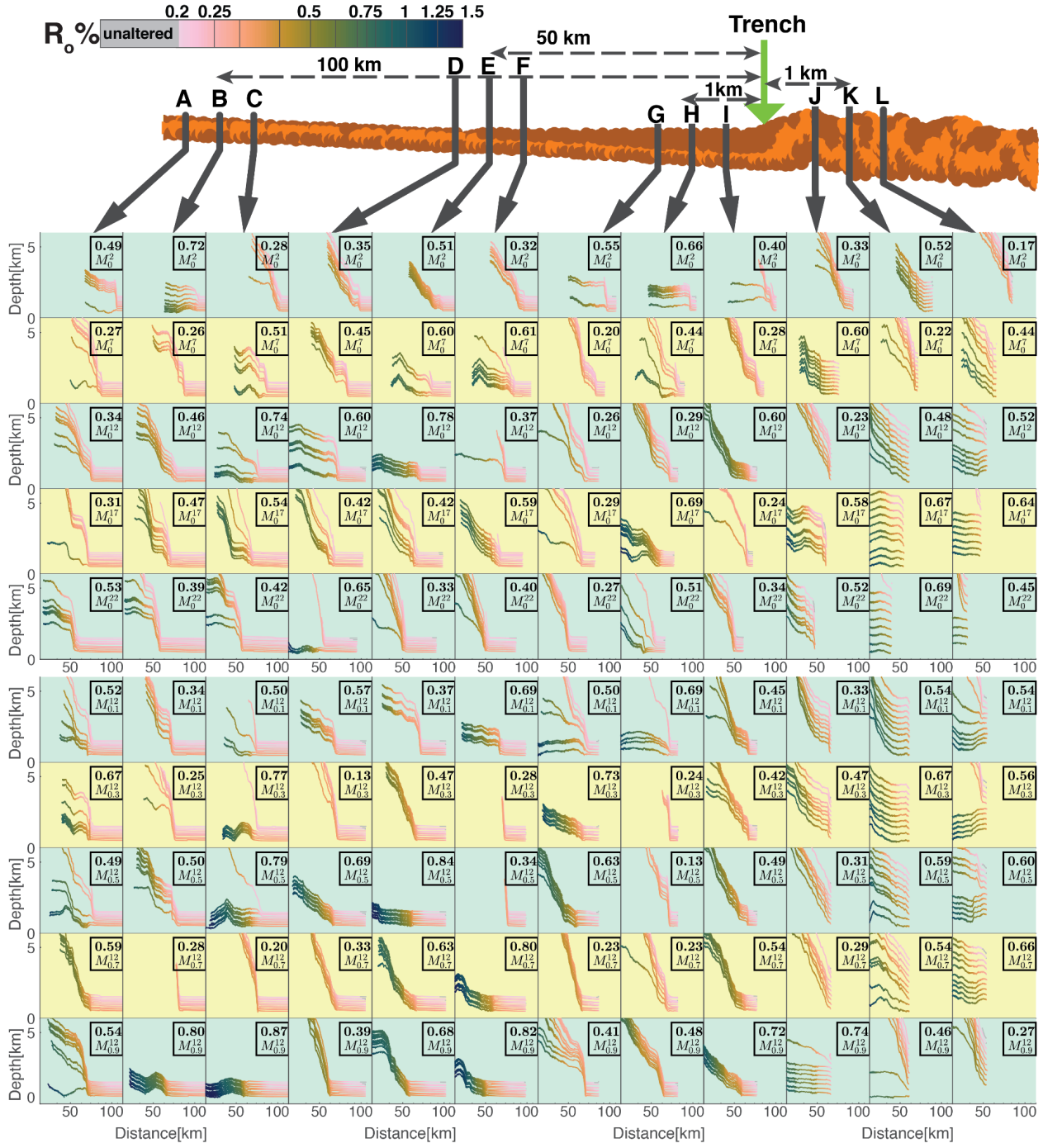

Fig. S6 *Vitrinite Reflectance(**%R$_0$**) vs Maximum Exposure temperature in models. Panel A,B and C show the Temperatures as a function of **%R$_0$** computed from Easy%R$_0$, Simple%R$_0$, Basin%R$_0$ for models* M_0^2-M_0^{22} . *Similarly panels D,E and F show the Temperatures as a function of **%R$_0$** computed from Easy%R$_0$, Simple%R$_0$, Basin%R$_0$ for models* $M_{0.1}^{12}$-$M_{0.9}^{12}$.

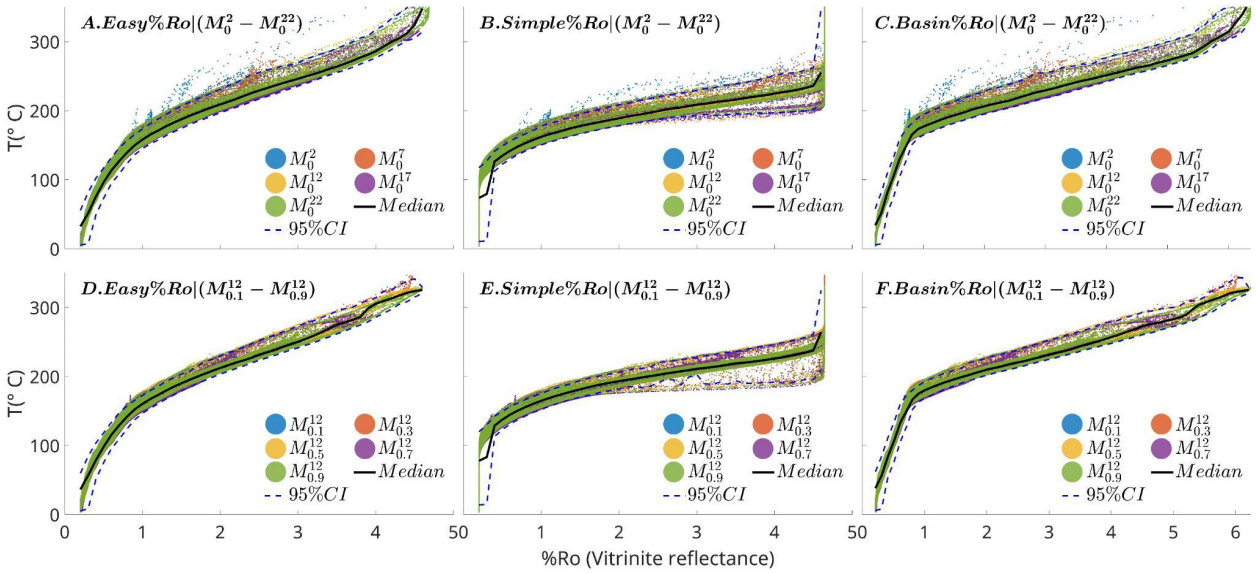

Fig. S7: %R_0 *vs T for model(shown by smaller markers) and C0002 borehole(shown by large circular markers) (Fukuchi et al., 2017).*